Cryobiology 115 (2024) 104879

Contents lists available at ScienceDirect

Cryobiology

journal homepage: www.elsevier.com/locate/cryo

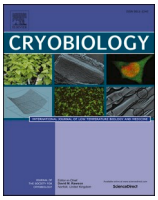

Cooling dynamics of droplets exposed to solid surface freezing and vitrification

Dejia Liu [a,b], Harriëtte Oldenhof [a,b], Xing Luo [c], Tobias Braun [a,b], Harald Sieme [b], Willem F. Wolkers [a,b,*]

[a] Biostabilization Laboratory - Lower Saxony Centre for Biomedical Engineering, Implant Research and Development, Hannover, Germany
[b] Unit for Reproductive Medicine - Clinic for Horses, University of Veterinary Medicine Hannover, Hannover, Germany
[c] Institute of Thermodynamics, Leibniz University Hannover, Garbsen, Germany

ARTICLE INFO

Keywords:
Cryopreservation
Vitrification
Numerical simulation
Solid surface vitrification/freezing
Droplet generation
Red blood cells

ABSTRACT

Solid surface freezing or vitrification (SSF/SSV) can be done by depositing droplets of a sample, e.g., cells in a preservation solution, onto a pre-cooled metal surface. It is used to achieve higher cooling rates and concomitant higher cryosurvival rates compared to immersion of samples into liquid nitrogen. In this study, numerical simulations of SSF/SSV were conducted by modeling the cooling dynamics of droplets of cryoprotective agent (CPA) solutions. It was assumed that deposited droplets attain a cylindrical bottom part and half-ellipsoidal shaped upper part. Material properties for heat transfer simulations including density, heat capacity and thermal conductivity were obtained from the literature and extrapolated using polynomial fitting. The impact of CPA type, i.e., glycerol (GLY) and dimethyl sulfoxide (DMSO), CPA concentration, and droplet size on the cooling dynamics was simulated at different CPA mass fractions at temperatures ranging from −196 to 25 °C. Simulations show that glycerol solutions cool faster compared to DMSO solutions, and cooling rates increase with decreasing CPA concentration. However, we note that material property data for GLY and DMSO solutions were obtained in different temperature and concentration ranges under different conditions, which complicated making an accurate comparison. Experimental studies show that samples that freeze have a delayed cooling response early on, whereas equilibration times are similar compared to samples that vitrify. Finally, as proof of concept, droplets of human red blood cells (RBCs) were cryopreserved using SSV/SSF comparing the effect of GLY and DMSO on cryopreservation outcome. At 20% (w/w), similar hemolysis rates were found for GLY and DMSO, whereas at 40%, GLY outperformed DMSO.

1. Introduction

Cryopreservation refers to long-term storage of cells, tissues, and organs at ultra-low subzero temperatures [1,2]. The challenge is to limit cryoinjury during the temperature trajectories from physiological temperatures down to low subzero temperatures, and back up again during rewarming. Different types of cryoinjuries are known that impair cellular viability and function. Cryopreservation strategies aim to mitigate cryoinjury by using cryoprotective agents, and optimized cooling and rewarming conditions. Conventional cryopreservation procedures typically involve the use of slow cooling rates, during which cells can sufficiently dehydrate upon extracellular ice formation therewith decreasing the likelihood of lethal intracellular ice formation [3]. Vitrification, on the other hand, is an emerging alternative method, which involves directly transforming the entire sample into a glassy state without the presence of ice [4].

Vitrification can be achieved in two ways; the first method involves increasing the CPA concentration to levels that prevent ice formation regardless of the cooling rate, which is known as equilibrium vitrification. The second method, referred to as non-equilibrium vitrification, relies on high cooling rates, allowing the use of lower concentrations of the CPA to reduce toxicity effects [5,6]. Moreover, CPA-free vitrification procedures have been reported, particularly for small volumes of sperm samples, but it should be noted that the absence of ice as proof of vitrification has not been demonstrated in most of these studies [7].

Vitrification tendency is predominantly governed by CPA concentration and cooling rate. Increasing the CPA concentration mitigates ice formation and promotes vitrification, but at the expense of a

* Corresponding author. Lower Saxony Centre for Biomedical Engineering, Implant Research and Development, Stadtfelddamm 34, 30625, Hannover, Germany.
E-mail address: willem.wolkers@tiho-hannover.de (W.F. Wolkers).

https://doi.org/10.1016/j.cryobiol.2024.104879
Received 26 September 2023; Received in revised form 14 February 2024; Accepted 29 February 2024
Available online 4 March 2024

concomitant increase in CPA toxicity [8]. Conversely, lower less toxic CPA concentrations require higher cooling rates to achieve the vitrified state [9].

For smaller sample sizes, droplet vitrification/freezing can be used, which is done in open systems, i.e., with samples that are not confined in containers. This can be done by either direct plunging of droplets (microliter sizes, containing cells/small tissues in CPA solution) into an immersion cooling liquid such as liquid nitrogen [10–12] or by depositing droplets onto a pre-cooled thermally conductive metal surface referred to as solid surface freezing or vitrification (SSF, SSV) [13–15]. Immersion of a sample in LN_2 causes the formation of a surrounding gas film (Leidenfrost effect), which impedes the cooling rate. Higher cooling rates and concomitant improved cryopreservation outcome can be achieved by SSF or SSV, which has been used for preservation of various cell types [15–17], embryos [18] and tissues [19].

Vitrification or ultra-rapid sample freezing during droplet deposition on a cold surface require efficient and homogeneous heat transfer to minimize temperature gradients within the sample. Heat transfer during SSF or SSV can be assessed by simulations if the material properties of the sample are known, particularly thermal conductivity, density and specific heat [20,21]. Thermal conductivity is a measure of a material's ability to conduct heat through molecular interactions. In liquids, these molecular interactions are relatively weak compared to crystalline solids, resulting in lower heat transfer efficiency, i.e., heat conductivity of ice is greater than that of water. Liquids with higher density have more densely packed molecules, resulting in improved molecular contact and more efficient heat transfer by conduction [22]. Material properties of CPA solutions exhibit temperature dependence, solution concentration dependence, and depend on specific intermolecular forces. Heat transfer simulations at cryogenic temperatures require extrapolation of material properties to desired temperature and concentration ranges [23,24].

The aim of this study was to investigate heat transfer during solid surface freezing/vitrification of droplets composed of various CPAs at different concentrations to estimate cooling rates at different sample positions. A previously described numerical simulation model [15] was further developed, which involved implementation of physical characteristics of dimethyl sulfoxide (DMSO) in addition to those of glycerol (GLY), and extension of physical properties to cover full concentration (0−1, w/w) and temperature (25 to −196 °C) ranges. This in turn was used to simulate the cooling behavior of 20-μL droplets composed of various mixtures of water/ice and GLY or DMSO. The temperature profile during droplet deposition was also assessed experimentally using a thermocouple, and the physical sample state was assessed using microscopy to identify the incidence of crystallization vs. vitrification. Finally, as proof of concept, droplets of human red blood cells were cryopreserved using SSV/SSF comparing the effect of GLY and DMSO on cryopreservation outcome.

2. Methods: mathematical modeling of rapid freezing of droplets on a cool solid surface

2.1. Modeling approach and droplet material properties: a methodological framework to investigate heat transfer during solid surface freezing

Droplets of a solution can be rapidly frozen or vitrified by solid surface freezing (SSV/SSF) by directly depositing the droplets on a pre-cooled metal block (e.g., copper or aluminum) placed in a polystyrene box filled with liquid nitrogen below the surface of the block, so that the surface temperature of the block approaches −196 °C. Droplets attain an ellipsoid-like shape on the surface of the block. Heat transfer simulations of droplet SSV/SSF require knowledge of material properties of both solvent and solutes as well as droplet dimensions.

A computational model was used to simulate the temperature profiles of droplets of different compositions and sizes during SSV/SSF. Fig. 1 shows a schematic framework of the procedure. The mathematical

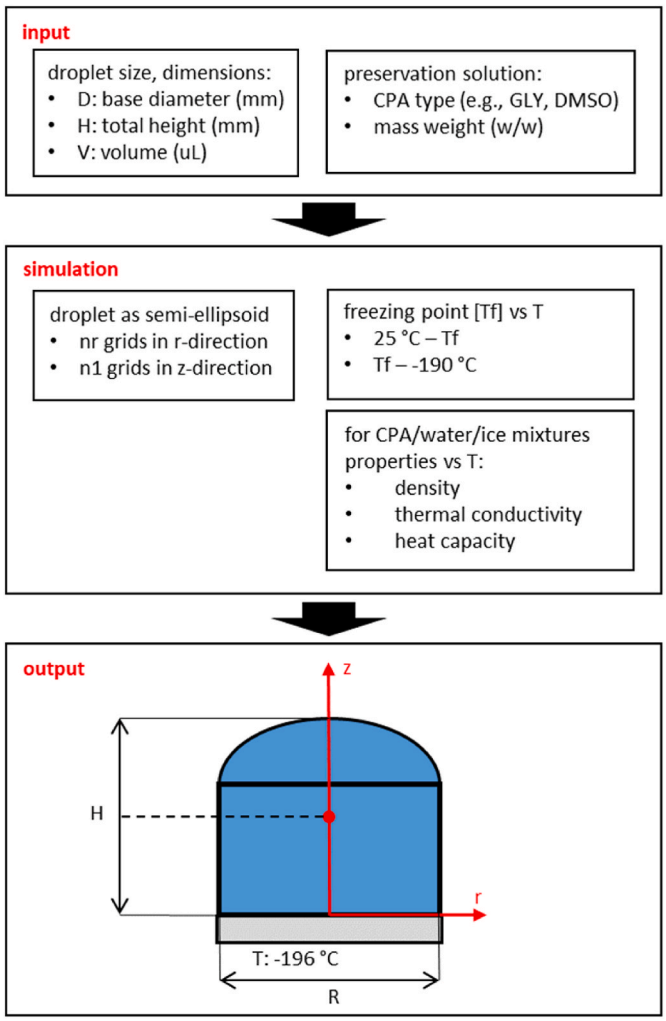

Fig. 1. Schematic flow chart presenting the procedure followed for simulations on temperature changes within droplets during rapid cooling on a cooled solid surface (i.e., SSF). It contains 'input', 'simulation' and 'output' modules. Input data include information concerning the droplet size, as well as CPA type and concentration employed. The simulation module processes the input data to depict the droplet with mesh coordinates, i.e., x-, y- and z-coordinates within a hemi ellipsoidal cap on a cylindrical base. In addition, using the equations described in the methods section, physical properties of the specific CPA solution (i.e., density, thermal conductivity, and heat capacity) are calculated as a function of time, i.e., during cooling of the specified droplet by means of heat transfer through conduction and convection. As output, the outcome of the simulation is presented three-dimensionally; as the temperature for each coordinate within the droplet as a function of the cooling process. This is done graphically for visualization, and all data points can be extracted for possibly plotting differently (e.g., temperature at a specific location versus time, different line plots for comparison).

simulation work is based on droplet input parameters, including dimensions (diameter, height, volume), CPA type (e.g., GLY, DMSO), and weight by mass (w/w), which are obtained from the experiment and previous reports. The droplet geometry in the simulation consists of a cylinder and a semi-ellipse with two semi-major axes R and R_z. The cylinder is divided into n_r grids in the r-direction and n_1 grids in the z-direction. The semi-ellipse is divided into n_2 grids in z direction. The freezing point temperatures at different glycerol mass fractions are used to separate the liquid-solid phase in the model, which has separate thermotropic physical properties (i.e., density, heat capacity, and thermal conductivity). Polynomial fitting was used for intra- and extrapolation and simulations at ultra-low temperatures over a wide

concentration range. The temperature distribution in the required time is shown as output figure.

The numerical simulation model was developed using MATLAB software (Mathworks). It was assumed that droplets that come in contact with a liquid-nitrogen-cooled metal block attain a composite structure comprising of a cylindrical base and hemi ellipsoidal cap. The ellipsoidal shaped surface of the object is defined by:

$$\frac{r^2}{R^2}+\frac{z^2}{R_z^2}=1, \quad \text{(Eq. 1)}$$

where R and R_z are the principal semi-axes of the ellipsoid in, respectively, the radial and axial direction. The height of the droplet is denoted as H. The volume V of the droplet can be expressed as:

$$V=\pi\left(\frac{RH}{R_z}\right)^2\left(R_z-\frac{H}{3}\right)=\pi R^2H_1+\frac{2}{3}\pi R^2(H-H_1), \quad \text{(Eq. 2)}$$

$$H_1=\left(\frac{3V}{\pi R^2}\right)^2-2H, \quad \text{(Eq. 3)}$$

where R represents the radius and H_1 the height of the cylinder.

Simulations were performed on droplets with volumes of 20 μL. Dimensions of droplets on a surface were obtained by microscopic inspection of high-resolution images of vitrified droplets; for 20 μL droplets, diameter: 3.52 mm, height: 2.64 mm.

2.2. Mathematical modeling of solid surface freezing: heat transfer by conduction and convection

Heat transfer from the cold bottom to the top of the droplet predominantly occurs by conduction. Material properties for heat transfer simulations including density, heat capacity and thermal conductivity, were obtained from the literature. Simulations were performed for different concentrations (GLY, DMSO; 0–1 [w/w] mass fractions) was, i.e., during cooling from 25 to −190 °C. Heat conduction is described as follows:

$$\rho c\frac{\partial T}{\partial t}=\nabla(\lambda\nabla T)=\frac{1}{r}\frac{\partial}{\partial r}\left(\lambda r\frac{\partial T}{\partial \tau}\right)+\frac{\partial}{\partial z}\left(\lambda\frac{\partial T}{\partial z}\right), \quad \text{(Eq. 4)}$$

$$t=0: T=T_a=22^{\circ}C, \quad \text{(Eq. 5)}$$

$$r=0:\frac{\partial T}{\partial r}=0, \quad \text{(Eq. 6)}$$

$$r=R, 0<z<H_1: -\lambda\frac{\partial T}{\partial r}=h_{per}(T-T_{N_2}), \quad \text{(Eq. 7)}$$

$$z=0: T=T_{LN}, \quad \text{(Eq. 8)}$$

$$r>H_1: -\lambda\frac{\partial T}{\partial n}=h_{top}(T-T_{N_2}). \quad \text{(Eq. 9)}$$

Here ρ is the density, c is the heat capacity, λ is the thermal conductivity, T is the droplet temperature in degrees Celsius, T_a the ambient temperature, T_{LN} and T_{N_2} the saturation temperature of nitrogen at ambient pressure and the surrounding nitrogen temperature, respectively, $T_{LN}=-196$ °C, $T_{N_2}=-190$ °C, h_{per} is heat transfer coefficient on the vertical peripheral surfaces of the cylinder. h_{top} is heat transfer coefficient on the top surface of the ellipsoid.

Heat transfer also occurs by convection at the droplet air interface. To calculate the contribution of convective heat transfer, it was assumed that the droplet volume and the area in contact with the ambient air did not change during cooling. For the natural convection heat transfer coefficients at the vertical peripheral surfaces of the cylinder, the mean Nusselt number is given, as follows [25]:

$$Nu_m=\frac{h_mL}{\lambda}=\left[0.825+0.387(f_1R_a)^{1/6}\right]^2, \quad \text{(Eq. 10)}$$

$$Ra_z=\frac{\beta g(t-t_{N_2})z^3}{\nu\kappa}, \quad \text{(Eq. 11)}$$

$$f_1=\left[1+\left(\frac{0.492}{Pr}\right)^{9/16}\right]^{-16/9}, \quad \text{(Eq. 12)}$$

The local Nusselt number can be obtained by the definition of the mean heat transfer coefficient:

$$h_m(z)=\frac{1}{z}\int_0^z h_m(z')dz', \quad \text{(Eq. 13)}$$

The natural convection heat transfer coefficients on the top surface of the ellipsoid h_{top} is calculated approximately with the following correlations for a heated flat plate:

$$Nu_{top}=\frac{h_{top}L}{\lambda}=\begin{cases}0.766(f_2Ra_{top})^{1/5}, f_2Ra_{top}<7\times10^4\\ 0.15(f_2Ra_{top})^{1/3}, f_2Ra_{top}\geq7\times10^4\end{cases}, \quad \text{(Eq. 14)}$$

$$Ra_{top}=\frac{\beta g(t-t_{N_2})(2R)^3}{\nu\kappa}, \quad \text{(Eq. 15)}$$

$$f_2=\left[1+\left(\frac{0.322}{Pr}\right)^{11/20}\right]^{-20/11}. \quad \text{(Eq. 16)}$$

Where L is the characteristic length, λ is thermal conductivity, R_a is Rayleigh number, β is coefficient of thermal expansion, g is gravitational acceleration, ν is kinematic viscosity, Pr is Prandtl number, κ is thermal diffusivity. The function f_1 describes the influence of the Prandtl Number in the entire range $0.001<Pr<\infty$. The function f_2 describes the influence of the Prandtl Number in the entire range $0<Pr<\infty$.

2.3. Freezing point temperature of GLY/water and DMSO/water mixtures

Fig. 2 presents previously reported data on the freezing point of aqueous GLY and DMSO solutions [26,27] for mass fractions (GLY/-water, DMSO/water, w, in w/w) ranging from 0 to 100%. Polynomial equations were used to determine the parameters describing the freezing point temperature during SSF. For w-values below and above the eutectic point (GLY: w, T_f: 0.67, −46.5 °C), the following equations were derived for the freezing temperature as a function of the glycerol concentration:

$$T_f=-115w^2+10.43w-1.05, (w\leq0.67), \quad \text{(Eq. 17)}$$

$$T_f=189.23w-172.04, (w>0.67), \quad \text{(Eq. 18)}$$

and for the freezing temperature as a function of the DMSO concentration:

$$T_f=-457.39w^2+70.899w-0.4876, (w\leq0.67), \quad \text{(Eq. 19)}$$

$$T_f=-598.71w^2+1491.9w-870.04, (w>0.67), \quad \text{(Eq. 20)}$$

where T_f is the freezing temperature (°C), and w the CPA mass fraction (w/w, -).

2.4. Temperature-dependence of the density of GLY/water/ice and DMSO/water/ice mixtures

The temperature dependence of the density of GLY/water solutions was derived from Ref. [28]:

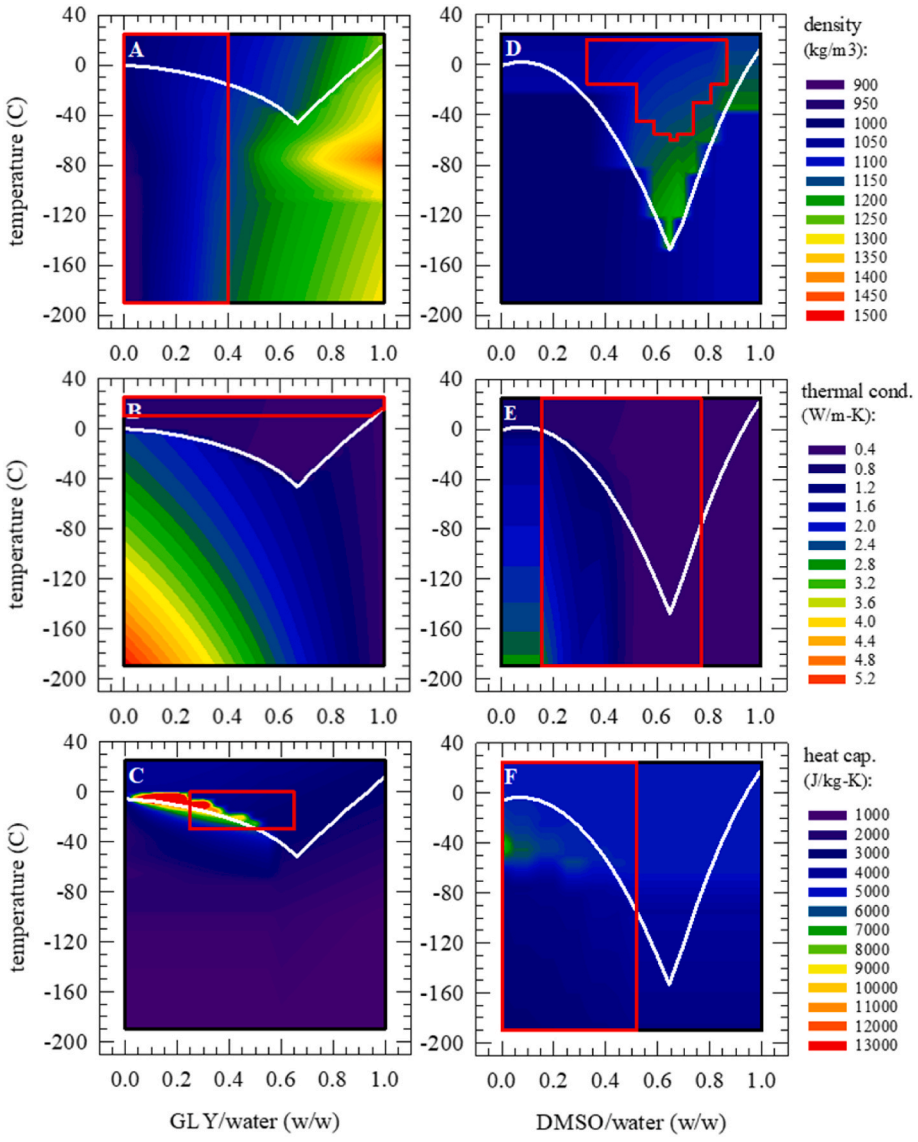

Fig. 2. Temperature and concentration-dependent changes in the density (A,D), thermal conductivity (B,E), and heat capacity (C,F) of mixtures composed of water/ice and GLY (A–C) or DMSO (D–F). Within three-dimensional plots these physical parameters are shown as colors (z-axis; with increasing values shifting from blue to red), versus both the CPA mass fraction (x-axis) and sample temperature (y-axis). The white line is added to indicate the freezing point of the solution versus the GLY and DMSO concentration. Ranges for which actual experimental values were found in the literature, are indicated with red boxes. Details concerning fitting of these data and inter/extrapolation to further ranges can be found in the method section. (For interpretation of the references to color in this figure legend, the reader is referred to the Web version of this article.)

$$\rho[GLY/water] = \kappa(T,w)\left[\rho_{water}(T) + \frac{\rho_{GLY}(T) - \rho_{water}(T)}{1 + \frac{\rho_{GLY}(T)}{\rho_{water}(T)}\left(\frac{1}{w} - 1\right)}\right], (T > T_f), \quad \text{(Eq. 21)}$$

where κ refers to the volume contraction coefficient, T to the sample temperature (°C), and ρ_{water} and ρ_{GLY} (in kg m^{-3}) represent the density of water and pure glycerol, respectively. The maximum relative deviation above the freezing temperature is 0.24% [29].

For GLY/ice mixtures, published data on the density at temperatures ranging from −273 to 25 °C. At approximately T < −123.15 °C, the solutions are in a glassy state and $\rho_{(T)}$ varies linearly with **temperature** [30]. Experimental data were fitted to derive intermediate values in this range. Table 1 shows the fitting equations for different concentrations. It should be noted that this gives values that are about 3% higher as reported elsewhere [31].

The temperature dependence of the density of DMSO/water solutions was obtained from Ref. [32]. Table 2 presents the coefficients for a least-squares quadratic fit of the density data to an equation of the form:

$$\rho[DMSO/water] = a + b(T + 273.15) + c(T + 273.15)^2, (T > T_f), \quad \text{(Eq. 22)}$$

where T refers to the sample temperature (°C), and $\rho[Me2SO/water]$ (in kg m^{-3}) represents the density of the DMSO/water mixture.

For DMSO/ice mixtures, no published data on the density were found. Therefore a mixture of the density of pure ice and pure DMSO is used as an approximation [33]. This is described by the following equations:

$$\rho_{ice} = 917 \times \left(1 - 1.17 \times 10^4 T\right), (-140°C \le T \le 0), \quad \text{(Eq. 23)}$$

$$\rho_{ice} = 930 \times \left(1 - 1.54 \times 10^5 T\right), (-140°C \le T \le -260°C), \quad \text{(Eq. 24)}$$

Table 1
Functions describing the density (ρ, in kg m^{-3}) of GLY/water mixtures, of different mass ratios (w/w, -), as a function of temperature (T, in °C). The equations were obtained by fitting previously reported data [30].

Concentration, w/w	Temperature range, °C	Polynomial approximation, °C	R^2 value
0	−78.02 to 25 °C	$1000.0274 - 0.0246 \times T - 0.0089 \times T^2 + 2.0777 \times 10^{-4} \times T^3 + 2.2631 \times 10^{-6} \times T^4$	0.9983
	−129.09 to −78.02 °C	$5196.1099 + 315.2217 \times T + 9.2122 \times T^2 + 0.1379 \times T^3 + 1.1241 \times 10^{-3} \times T^4 + 4.7552 \times 10^{-6} \times T^5 + 8.1871 \times 10^{-9} \times T^6$	0.9443
	−190 to −129.78 °C	$921.9544 - 0.1431 \times T$	0.9910
0.007	−70.38 to 25 °C	$1002.3770 - 0.0287 \times T - 8.9104 \times 10^{-3} \times T^2 + 1.4634 \times 10^{-4} \times T^3 + 1.6005 \times 10^{-6} \times T^4$	0.9969
	−132.34 to −70.38 °C	$-1484.2145 - 132.0848 \times T - 2.8054 \times T^2 - 0.0292 \times T^3 - 1.4888 \times 10^{-4} \times T^4 - 2.9869 \times 10^{-7} \times T^5$	0.8267
	−190 to −132.34 °C	$932.1983 - 0.1390 \times T$	0.9972
0.05	−71.44 to 25 °C	$1011.5247 - 0.0104 \times T - 7.7934 \times 10^{-3} \times T^2 + 2.1962 \times 10^{-5} \times T^3 - 4.9517 \times 10^{-7} \times T^4 - 6.5162 \times 10^{-9} \times T^5$	0.9982
	−86.93 to −71.44 °C	$1595.4129 + 21.6316 \times T + 0.2433 \times T^2 + 8.9589 \times 10^{-4} \times T^3$	0.9930
	−190 to −86.93 °C	$951.5931 - 0.1588 \times T$	0.9983
0.10	−71.66 to 25 °C	$1024.7808 - 0.1363 \times T - 0.0103 \times T^2 - 2.1962 \times 10^{-5} \times T^3 + 3.2618 \times 10^{-6} \times T^4 + 1.1832 \times 10^{-7} \times T^5 + 1.0738 \times 10^{-9} \times T^6$	0.9988
	−147.73 to −71.66 °C	$3241.1627 + 139.2462 \times T + 3.4923 \times T^2 + 0.0454 \times T^3 + 3.2255 \times 10^{-4} \times T^4 + 1.1932 \times 10^{-6} \times T^5 + 1.7990 \times 10^{-9} \times T^6$	0.9398
	−190 to −147.73 °C	$982.6845 - 0.1595 \times T$	0.9968
0.14	−78.15 to 25 °C	$1036.5675 - 0.2529 \times T - 6.9218 \times 10^{-3} \times T^2 + 1.2346 \times 10^{-4} \times T^3 + 1.5947 \times 10^{-6} \times T^4$	0.9900
	−138.19 to −78.15 °C	$6800.9187 + 271.0212 \times T + 5.0060 \times T^2 + 0.0456 \times T^3 + 2.0559 \times 10^{-4} \times T^4 + 3.6623 \times 10^{-7} \times T^5$	0.9973
	−190 to −138.19 °C	$1002.8215 - 0.1642 \times T$	0.9958
0.17	−87.10 to 25 °C	$1045.2517 - 0.2597 \times T - 3.4281 \times 10^{-3} \times T^2 + 3.0553 \times 10^{-5} \times T^3 - 8.9152 \times 10^{-7} \times T^4 - 1.0638 \times 10^{-8} \times T^5$	0.9932
	−108.02 to −87.10 °C	$1015.5084 - 0.1107 \times T$	0.7494
	−190 to −87.02 °C	$1007.7937 - 0.1810 \times T$	0.9978
0.21	−58.24 to 25 °C	$1055.2128 - 0.3507 \times T - 1.1853 \times 10^{-3} \times T^2 + 1.4844 \times 10^{-4} \times T^3 - 8.2468 \times 10^{-7} \times T^4 - 7.6155 \times 10^{-8} \times T^5 - 5.6113 \times 10^{-10} \times T^6$	0.9928
	−88.40 to −58.24 °C	$110762.1358 + 9141.1887 \times T + 316.0645 \times T^2 + 5.8043 \times T^3 + 0.0597 \times T^4 + 3.2626 \times 10^{-4} \times T^5 + 7.3974 \times 10^{-7} \times T^6$	0.9379
	−190 to −88.40 °C	$1040.1057 - 0.1842 \times T$	0.9978
0.28	−32.92 to 25 °C	$1072.9442 - 0.4439 \times T - 4.1094 \times 10^{-3} \times T^2 + 2.7729 \times 10^{-4} \times T^3 + 1.4677 \times 10^{-5} \times T^4 - 4.5228 \times 10^{-7} \times T^5 - 1.7565 \times 10^{-8} \times T^6$	0.9987
	−120.95 to −32.92 °C	$1032.5056 - 7.4123 \times T - 0.3669 \times T^2 - 0.0085 \times T^3 - 1.0009 \times T^4 - 5.8558 \times 10^{-7} \times T^5 - 1.3480 \times 10^{-9} \times T^6$	0.9196
	−190 to −120.95 °C	$1064.8381 - 0.2204 \times T$	0.9969
0.36	−73.09 to 25 °C	$1094.1821 - 0.4292 \times T - 2.0140 \times 10^{-3} \times T^2 - 2.0161 \times 10^{-5} \times T^3 - 2.6459 \times 10^{-7} \times T^4$	0.9980
	−108.38 to −73.09 °C	$7757.7331 + 297.9740 \times T + 4.9511 \times T^2 + 0.0362 \times T^3 + 9.8140 \times 10^{-5} \times T^4$	0.9572
	−190 to −108.38 °C	$1112.3455 - 0.2199 \times T$	0.9984
0.43	−69.77 to 25 °C	$1113.1695 - 0.5886 \times T - 2.6808 \times 10^{-3} \times T^2 + 8.9262 \times 10^{-5} \times T^3 + 1.6696 \times 10^{-6} \times T^4$	0.9980
	−98.02 to −69.77 °C	$1592.7740 + 15.9310 \times T + 0.1874 \times T^2 + 7.2327 \times 10^{-4} \times T^3$	0.8811
	−190 to −98.02 °C	$1125.3394 - 0.2370 \times T$	0.9989

Table 2
Functions describing the density (ρ, in kg m^{-3}) of DMSO/water mixtures, of different mass ratios (w/w, -), as a function of temperature (T, in °C). The equations resulted from fitting previously reported experimental data with the relative error ($\Delta\rho/\rho$) of each density ±0.12% [32].

X_{DMSO}	a	$b \times 10^4$	$c \times 10^7$	Temperature range, T, °C	Temperature range, T+273.15, °K
0.33	1.107	1.003	−10.62	−15.15-19.85	258–293
0.52	1.219	−2.075	−9.618	−45.15-19.85	228–293
0.59	1.295	−6.310	−2.784	−55.15-19.85	218–293
0.65	1.338	−8.290	−0.3393	−60.15-19.85	213–293
0.68	1.425	−14.80	12.14	−55.15-19.85	218–293
0.70	1.338	−7.906	−1.222	−55.15-19.85	218–293
0.74	1.346	−7.568	−2.940	−55.15-19.85	218–293
0.81	1.414	−11.81	4.132	−30.15-19.85	243–293
0.87	1.575	−22.28	24.51	−10.15-19.85	263–293

$$\rho_{[DMSO/ice]} = \rho_{DMSO,25°C} w_{DMSO} + \rho_{ice}(1 - w_{DMSO}), \left(T \le T_f\right). \quad \text{(Eq. 25)}$$

2.5. Temperature-dependence of the thermal conductivity of GLY/water/ice and DMSO/water/ice mixtures

The thermal conductivity of aqueous glycerol increases with increasing water content, which has been described for temperatures ranging from 10 to 80 °C [34]. These data were fitted using bivariate polynomials to obtain the thermal conductivity (λ, in W m^{-1} K^{-1}) as:

$$\lambda[GLY/water] = A(w) + B(w)T, \left(T > T_f\right), \quad \text{(Eq. 26)}$$

$$A(w) = 418.4 \times \left(1.34 \times 10^{-3} - 7.94 \times 10^{-4} w - 5.44 \times 10^{-6} w^2 + 1.37 \times 10^{-4} w^3\right), \quad \text{(Eq. 27)}$$

$$B(w) = 418.4 \times \left(3.67 \times 10^{-6} - 6.52 \times 10^{-6} w + 2.65 \times 10^{-5} w^2 - 1.09 \times 10^{-4} w^3 + 1.92 \times 10^{-4} w^4 - 1.54 \times 10^{-4} w^5 + 4.72 \times 10^{-5} w^6\right), \quad \text{(Eq. 28)}$$

with $A(w)$ and $B(w)$ referring to the polynomials of the glycerol mass fraction dependence.

No thermal conductivity data were found for GLY/ice mixtures. Therefore, values were approximated from the relative contributions of pure water and vitreous glycerol. The thermal conductivity of vitreous glycerol at −78 °C ($\lambda_{GLY,-78°C}$) was taken as 0.318 W m^{-1} K^{-1} [34]. Engineering ToolBox 2021 [35] was used to derive λ_{ice} at varying temperature. The thermal conductivity of the mixture is then described by:

$$\lambda[GLY/ice] = (1-w)\lambda_{ice} + \lambda_{GLY,-78°C}w, \left(T \le T_f\right), \quad \text{(Eq. 29)}$$

$$\lambda_{ice} = 4\times10^{-5}T^2 - 0.0093T + 2.2008. \quad \text{(Eq. 30)}$$

It can be seen from Table 3 that the thermal conductivity of aqueous DMSO decreases with increasing concentration for temperatures ranging from −180 to 37.7 °C. For DMSO/water mass fractions greater than 0.52 w/w, complete vitrification occurs, as evidenced by a monotonic decrease in thermal conductivity with decreasing temperature. Crystallization was evident at DMSO concentrations of 0.52 w/w, resulting in a significant increase in thermal conductivity as crystallization progressed. The thermal conductivity of DMSO follows opposite trends in the vitrified and crystallized phases, the latter increasing with decreasing temperature [36].

2.6. Temperature-dependence of the heat capacity of GLY/water/ice and DMSO/water mixtures

Two reports were found describing heat capacity of GLY/water/ice mixtures, i.e., for 0.25–0.65 mass fractions in the −32 to 2 °C temperature range [37], and for 0.25–0.40 mass fractions with temperatures ranging from −140 to 25 °C [38]. In the latter study, both the liquid and ice phases were included in the calculations. For GLY/water mass fractions ranging from 0 to 0.55, and temperatures between T_f to 80 °C range [37], the heat capacity (c, in J kg^{-1} K^{-1}) was fitted for describing as:

$$c[GLY/water] = A(w) + B(w)T, \quad \text{(Eq. 31)}$$

$$A(w) = 3746.12 + 309.97w - 2365.81w^2, \quad \text{(Eq. 32)}$$

$$B(w) = 5.93 + 17.15w, \quad \text{(Eq. 33)}$$

where $A(w)$ and $B(w)$ refer to the polynomials dependent on the glycerol mass fraction.

For the same GLY/water/ice mass fractions ranging from 0 to 0.55 and temperatures ranging from $-31.67 - T_f$ °C [37] the heat capacity is described as:

$$c[GLY/ice] = A(T) + B(T)w, \quad \text{(Eq. 34)}$$

$$A(T) = 2705.50 + 82.85T + 4.62T^2 + 0.14T^3 + 1.54\times10^{-3}T^4, \quad \text{(Eq. 35)}$$

$$log_{10}[B(T)] = 6.37 + 0.27T + 0.01T^2 + 3.90\times10^{-4}T^3 + 3.93\times10^{-6}T^4, \quad \text{(Eq. 36)}$$

where $A(T)$ and $B(T)$ refer to the polynomials dependent on the temperature.

For the same GLY/water/ice mass fractions ranging from 0 to 0.55 and temperatures ranging from −190 – −31.67 °C [37] the heat capacity is described as:

$$c[GLY/ice] = 1965.43 + 6.87T, T \le -100.31°C, \quad \text{(Eq. 37)}$$

$$c[GLY/ice] = -24813.78 - 1591.46T - 28.93T^2 - 0.13T^3 + 1.08\times10^{-3}T^4 + 8.34\times10^{-6}T^5, -100.31°C \le T \le -75.48°C, \quad \text{(Eq. 38)}$$

$$c[GLY/ice] = c_{0.25}(T) + \frac{c_{0.4}(T) - c_{0.25}(T)}{0.4 - 0.25}(w - 0.25), -75.48°C \le T \le -31.67°C, \quad \text{(Eq. 39)}$$

$$c_{0.25}(T) = 3675.15 + 104.58\left(T+\frac{95}{3}\right) + 4.29\left(T+\frac{95}{3}\right)^2 + 4.18\times10^{-2}\left(T+\frac{95}{3}\right)^3 - 4.72\times10^{-3}\left(T+\frac{95}{3}\right)^4 - 1.47\times10^{-4}\left(T+\frac{95}{3}\right)^5 - 1.18\times10^{-6}\left(T+\frac{95}{3}\right)^6, \quad \text{(Eq. 40)}$$

$$c_{0.4}(T) = 4800.79 + 161.81\left(T+\frac{95}{3}\right) + 8.84\left(T+\frac{95}{3}\right)^2 + 0.62\left(T+\frac{95}{3}\right)^3 + 3\times10^{-2}\left(T+\frac{95}{3}\right)^4 + 7.15\times10^{-4}\left(T+\frac{95}{3}\right)^5 + 6.28\times10^{-6}\left(T+\frac{95}{3}\right)^6, \quad \text{(Eq. 41)}$$

where $c_{0.25}(T)$ and $c_{0.4}(T)$ refer to the temperature dependency heat capacity in 0.25 and 0.4 mass fraction.

While the heat capacity in (J kg^{-1} K^{-1}) of glycerol for mass fraction ranging from 0.55 to 1 (w/w) as experimentally determined and described elsewhere [37] was fitted using:

$$c = A(w) + 16.797T, -100 \le T \le 25°C, \quad \text{(Eq. 42)}$$

$$A(w) = -1579.9w + 4108.6, \quad \text{(Eq. 43)}$$

$$c = A(w) + 6.87(T+100), -190 \le T \le 100°C, \quad \text{(Eq. 44)}$$

$$A(w) = -1579.9w + 2428.9, \quad \text{(Eq. 45)}$$

where A(w) and B(w) refer to the polynomials dependent on the glycerol mass fraction.

For DMSO/water mass fractions ranging 0–0.52 and temperatures ranging −273.15–25 °C, heat capacity data were found [39] and fitted by the equations in Table 4. The heat capacity data were obtained from molecular dynamics simulations assuming DMSO-water systems vitrify.

For both 20% and 40% GLY as well as DMSO, thermal diffusivity (α) is calculated using the following equation:

$$\alpha = \frac{\lambda}{\rho c} \quad \text{(Eq. 46)}$$

We note that the simulation model that was used here will be made available to interested scientists upon reasonable request.

3. Methods: experimental procedures

3.1. Temperature profiles of droplets deposited on a pre-cooled solid surface

To experimentally determine cooling rates during droplet freezing on a solid surface, a 53 II digital thermometer (Fluke) was used with a thermocouple consisting of a type T fine gage bare wire (1 mm in diameter). The wire was positioned on a copper block (50 × 110 × 85 mm; Sürth Metall-und Stahlhandel), which was kept in a polystyrene box (370 × 200 × 220 mm) filled with liquid nitrogen up to 50 mm below the surface of the block. Solutions composed of different DMSO/water and GLY/water mass fractions (w/w: 0.2 and 0.4) were prepared and tested, similarly as done for the simulations, while buffered saline (PBS; 137 mM NaCl, 2.7 mM KCl, 10 mM Na_2HPO_4, 1.8 mM KH_2PO_4, pH 7.4) was included for comparison. Room temperature (~22 °C) droplets of 20 μL were generated using a micropipette and released about 5 mm above the cooled block, depositing the droplet directly on the thermocouple wire while recording the temperature at 1 s intervals. This predominantly captures the temperature profile at the bottom of the droplet when it hits the block. The temperature of the pre-cooled block surface was determined to be −170 °C. Sample temperature typically started at −170 °C followed by a temperature increase (i.e., initial block-droplet contact) and a subsequent temperature decrease until reaching the equilibrium temperature of the surface.

3.2. Droplet cryopreservation of red blood cells

The solid surface freezing set up described above was tested using red blood cells by depositing droplets of red blood cells on the pre-cooled metal block. Whole blood samples from four anonymized healthy donors were provided by the Institute for Transfusion Medicine of the Hannover Medical School. The procedures described in this work were ethically approved, and according to federal regulations. Whole blood was centrifuged (500×*g*, 5 min), where after the supernatant and interface layers were removed. The recovered red blood cells (RBCs) were washed three times with PBS.

To prepare RBC samples with varying DMSO and GLY concentrations, RBC/PBS suspensions were centrifuged (2000×*g*, 5 min) and resuspended in 1 mL PBS. The cell concentration was determined using a Neubauer haemocytometer. Then, 0.300 mL was transferred to a microtube that contained a bottom layer of 0.300 mL 60% GLY-or-DMSO/PBS and a 0.300 mL PBS upper layer; as described by Rogers et al., in 2018. After immediate mixing, this gives a 0.900 mL sample

Table 3
Functions describing the best-fit polynomial approximation data for the thermal conductivity of DMSO/water/ice mixture of different mass ratios (w/w, -), as a function of temperature (T, in °C). The equations resulted from fitting previously reported experimental data [36].

Concentration, w/w	Temperature range, °C	Polynomial approximation, °C	R^2 value
0.15	−180 to −9.4 °C	$7.63\times10^{-10}\times T^4+1.60\times10^{-7}\times T^3+9.58\times10^{-6}\times T^2-6.01\times10^{-3}\times T+1.32$	0.981
	−9.4 to −0.2 °C	$1.41\times10^{-3}\times T^2-6.86\times10^{-2}\times T+0.606$	0.991
0.23	−180 to −17.5 °C	$-1.55\times10^{-9}\times T^4-5.81\times10^{-7}\times T^3-8.01\times10^{-5}\times T^2-9.82\times10^{-3}\times T+0.9$	0.996
	−17.5 to −11.5 °C	$-3.97\times10^{-3}\times T^2-1.40\times10^{-1}\times T-0.184$	
	−11.5 to −5.4 °C	$-3.47\times10^{-3}\times T^2-1.25\times10^{-1}\times T-0.0792$	
	−5.4 to 18.2 °C	$1.94\times10^{-3}\times T+0.504$	
0.30	−180 to −24.2 °C	$-1.44\times10^{-9}\times T^4-6.42\times10^{-7}\times T^3-1.08\times10^{-4}\times T^2-1.16\times10^{-2}\times T+0.567$	0.997
	−24.2 to −17.3 °C	$-2.11\times10^{-3}\times T^2-1.06\times10^{-1}\times T-0.535$	
	−17.3 to −13.6 °C	$-1.97\times10^{-4}\times T^3-1.51\times10^{-2}\times T-3.89\times10^{-1}\times T-2.56$	
	−13.6 to 8.4 °C	$-1.93\times10^{-3}\times T+0.458$	
0.38	−180 to −32.7 °C	$-4.48\times10^{-10}\times T^4-2.76\times10^{-7}\times T^3-6.58\times10^{-5}\times T^2-1.16\times10^{-2}\times T+0.445$	0.997
	−32.7 to −19.2 °C	$-9.77\times10^{-4}\times T^2-7.15\times10^{-2}\times T-0.6$	
	−19.2 to 20.6 °C	$1.23\times10^{-3}\times T-0.434$	0.916
0.45	−180 to −47.3 °C	$-6.65\times10^{-10}\times T^4-3.94\times10^{-7}\times T^3-1.01\times10^{-5}\times T^2-1.31\times10^{-2}\times T+0.0931$	0.971
	−47.3 to −37.7 °C	$-3.85\times10^{-4}\times T^2-3.97\times10^{-2}\times T-0.491$	
	−37.7 to −32.0 °C	$-6.27\times10^{-4}\times T^2-5.98\times10^{-2}\times T-0.906$	
	−32.0 to18.5 °C	$9.25\times10^{-4}\times T+0.396$	0.932
0.52	−180 to 25.5 °C	$-2.95\times10^{-10}\times T^4-6.87\times10^{-8}\times T^3-1.29\times10^{-6}\times T^2+7.42\times10^{-4}\times T+0.356$	0.982
0.59	−180 to 17.2 °C	$-2.41\times10^{-10}\times T^4-5.76\times10^{-8}\times T^3-2.31\times10^{-6}\times T^2+5.57\times10^{-4}\times T+0.323$	0.989
0.67	−180 to 22.3 °C	$-2.02\times10^{-10}\times T^4-4.57\times10^{-8}\times T^3-1.90\times10^{-6}\times T^2+3.25\times10^{-4}\times T+0.301$	0.948
0.77	−180 to 13.8 °C	$-1.14\times10^{-10}\times T^4-1.50\times10^{-8}\times T^3+1.07\times10^{-6}\times T^2+3.74\times10^{-4}\times T+0.287$	0.987

Table 4
Functions describing the heat capacity (*c*, in J kg^{-1} K^{-1}) of DMSO/water mixtures at seven different mass ratios (0, 0.08, 0.19, 0.27, 0.37, 0.45, 0.52, w/w), as a function of temperature (*T*, in °C). The equations were obtained by fitting previously reported data [39].

Concentration, w/w	Temperature range, °C	Polynomial approximation, °C	R^2 value
0	−25 to 25 °C	$0.3632\times T^2-15.205\times T+5221.7$	0.980
	−40 to −25 °C	$-175.23\times T+749.07$	0.967
	−70 to −40 °C	$194.12\times T+16225$	0.978
	−190 to −70 °C	$2.4266\times T+3364.4$	0.829
0.08	−45 to 25	$0.3374\times T^2-9.2554\times T+5124.2$	0.955
	−75 to −45	$108.65\times T+11487$	0.978
	−190 to −75	$0.0113\times T^2+7.217\times T+3908.5$	0.945
0.19	−20 to 25	$0.0778\times T^2-3.2605\times T+5095.4$	0.969
	−40 to −20	$-40.965\times T+4074.8$	0.999
	−70 to −40	$85.379\times T+9629.6$	0.870
	−190 to −70	$0.0111\times T^2+7.2154\times T+3957.6$	0.958
0.27	−50 to 25	$0.0496\times T^2-2.385\times T+5114.3$	0.687
	−80 to −50	$87.298\times T+10474$	0.981
	−190 to −80	$3.9046\times T+3524.7$	0.926
0.37	−25 to 25	$-0.1731\times T+5089.8$	0.008
	−45 to −25	$-14.096\times T+4590.2$	0.723
	−70 to −45	$40.029\times T+7346.8$	0.969
	−190 to −70	$0.0143\times T^2+11.228\times T+4775.4$	0.956
0.45	−50 to 25	$0.0642\times T+5044$	0.001
	−80 to −50	$52.438\times T+8286.3$	0.942
	−190 to −80	$5.7845\times T+4340.1$	0.928
0.52	−55 to 25	$0.3847\times T+5033$	0.090
	−95 to −55	$35.239\times T+7252.3$	0.950
	−190 to −95	$8.0002\times T+4874.8$	0.963

containing RBCs and 20% GLY or DMSO. This sample was further diluted and mixed with 0.900 mL 20 or 60% GLY-or-DMSO/PBS to obtain RBC/PBS samples ($70-105 \times 10^6$ cells mL^{-1}) supplemented with either 20 or 40% final concentrations of GLY and DMSO. RBCs diluted in PBS without CPAs were used as control.

For each preparation, minimally five 20-μL droplets per treatment group were subjected to freezing/vitrification on a solid surface as described in detail above. The appearance of the droplets was checked (frozen/vitrified), where after they were collected and maintained in tubes in liquid nitrogen (minimally 30 min) until thawing/warming, which was done by direct transfer of frozen/vitrified droplets (5 per treatment group; 0.100 mL total) in 0.900 mL solution of 37 °C. To prevent osmotic shock, the same CPA solution was used in which the RBCs were present, i.e., PBS supplemented with 0–40% GLY or DMSO. Samples (0.100 mL) diluted in 0.900 mL were taken as pre-freeze control.

After thawing/warming, samples were centrifuged (2000×*g*, 5 min), at 22 °C, and the supernatants were transferred into a 96-well plate. The absorbance at 541 nm was taken as a measure for hemolysis, i.e., with respect to maximum hemolysis as determined after adding Triton X-100

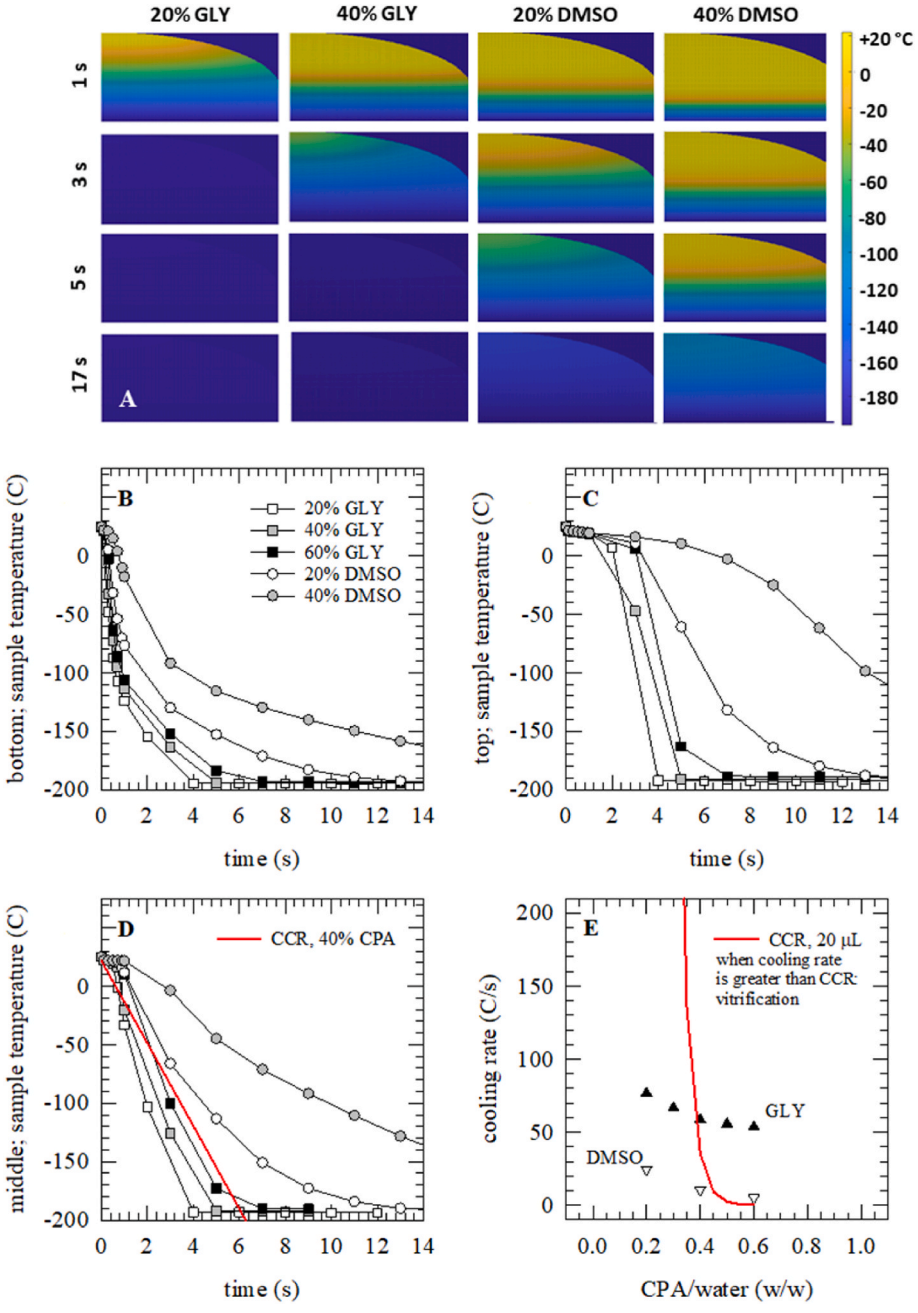

Fig. 3. Outputs of simulations performed, of rapid cooling of droplets (20-μL) of different compositions (20−60% GLY and DMSO) upon depositing on a liquid-nitrogen-cooled surface. Panel A shows temperature distributions within the droplets (i.e., cross section in the middle); for 20 and 40% GLY as well as DMSO at distinct time points (1, 3, 5 and 17 s). From such simulation plots, the sample temperature in the middle (r,z: 0,0) at different z-locations was derived, i.e., at the bottom (B), top (C), and the center (D) of the droplet with respect to the cooled block; for plotting versus the cooling time, for GLY (squares) and DMSO (circles) of different concentrations (20%: white, 40%: grey, 60%: black). From this, for the middle position, the cooling rate was estimated and plotted versus the GLY/DMSO concentration (panel E). In addition, plots on the calculated critical cooling rate (CCR) for attaining a vitrified state are presented (red lines), i.e., for 20 μL droplets of 40% CPA (D) as well as varying CPA concentration (E). (For interpretation of the references to color in this figure legend, the reader is referred to the Web version of this article.)

(50 μL 100% (v/v) Triton-X100, added to 0.850 mL PBS supplemented with 0.100 mL RBC/PBS).

4. Results

4.1. Temperature and concentration dependent changes in density, thermal conductivity and heat capacity

Physical property data of mixtures of water/ice and GLY as well as DMSO were obtained from the literature and presented graphically in Supplemental Fig. 1. Data were used for inter- and extrapolation to cover full concentration and temperature ranges needed for simulations. Fig. 2 presents a three-dimensionally visualized outcome of the density, thermal conductivity, and heat capacity of mixtures of water/ice and GLY or DMSO as a function of solute concentration and temperature. The freezing curve is added to show the effect of the liquid-crystalline phase transition (and vice versa) on the material properties. At low solute concentrations, densities depict an abrupt change during the water to ice phase transition, which diminishes at higher solute concentration. At low temperatures, density values increase with increasing GLY and DMSO concentration. Furthermore, at low temperatures densities appear to be higher for GLY than for DMSO water/ice mixtures, especially around −80 °C (Fig. 2A–D). Thermal conductivity increases with decreasing temperature and solute concentration, which is particularly evident for GLY water/ice mixtures (Fig. 2B–E). The heat capacity increases during the water-ice phase change, and the magnitude of this event (i.e., due to the latent heat of fusion) decreases with increasing solute concentration (Fig. 2C). For low concentration DMSO/water mixtures a similar peak is seen, however, here the temperature range falls slightly below the melting temperature (Fig. 2F). Below the melting point, the heat capacity appears to linearly decrease with decreasing temperature. We note that the heat capacity data for DMSO/water mixtures were derived from molecular dynamics simulations assuming samples vitrify (do not freeze).

4.2. Heat transfer during droplet deposition on a cold surface

A numerical model was developed to simulate heat transfer dynamics within droplets during deposition on a cold surface. Droplets of 20-μL were assumed to attain a semi-ellipsoidal shape on the surface, with a 3.5 mm base diameter and 2.6 mm height. Fig. 3A shows a visualization of the cooling process, for 20 and 40% (w/w), GLY and DMSO, starting from the initial droplet temperature (25 °C) down to −190 °C, i.e., when the droplet comes into contact with the liquid-nitrogen-cooled solid surface. Initially a temperature gradient is visible within the droplet, with the lowest temperatures at the bottom, closest to the surface, while moving as a front to the top of the droplet versus time. The time needed to entirely cool a droplet depends on its composition. Droplets containing lower CPA mass fractions, appear to cool faster. Furthermore, GLY droplets cool faster than DMSO droplets; it takes about 3 s to entirely cool a 20-μL droplet composed of 20% GLY compared to about 17 s for a 20% DMSO droplet.

Temperature profiles were extracted from simulation outputs at different locations within the droplet; namely at the bottom, top and center (Fig. 3B–D). This further illustrates the non-uniform temperature distribution and cooling profiles within the droplets, as well as composition-dependent differences between DMSO and GLY. For the middle position of the droplet, the cooling rate was estimated from the linear region, and plotted versus the GLY and DMSO concentration (Fig. 3E). When comparing the simulated cooling rates with the predicted critical cooling rate curve, it can be seen that concentrations of approximately 40% and higher are likely to lead to vitrification.

4.3. Experimental assessment of cooling rates during droplet deposition

Temperature profiles during SSV/SSF were also assessed experimentally using thermocouple measurements (Fig. 4) to corroborate the simulated cooling profiles, while the incidence of vitrification vs. freezing was visually inspected. After deposition and equilibration, droplets composed of 40% GLY appear clear and vitrified, 40% DMSO droplets appear partially vitrified, whereas droplets composed of 20% GLY or DMSO appear opaque and frozen. A thermocouple wire was placed on a liquid-nitrogen-cooled copper block to monitor the temperature of a 20-μL droplet deposited directly on the thermocouple on the block. The initial temperature corresponds to that of the block (i.e., −170 °C), after which the temperature rapidly increases when the

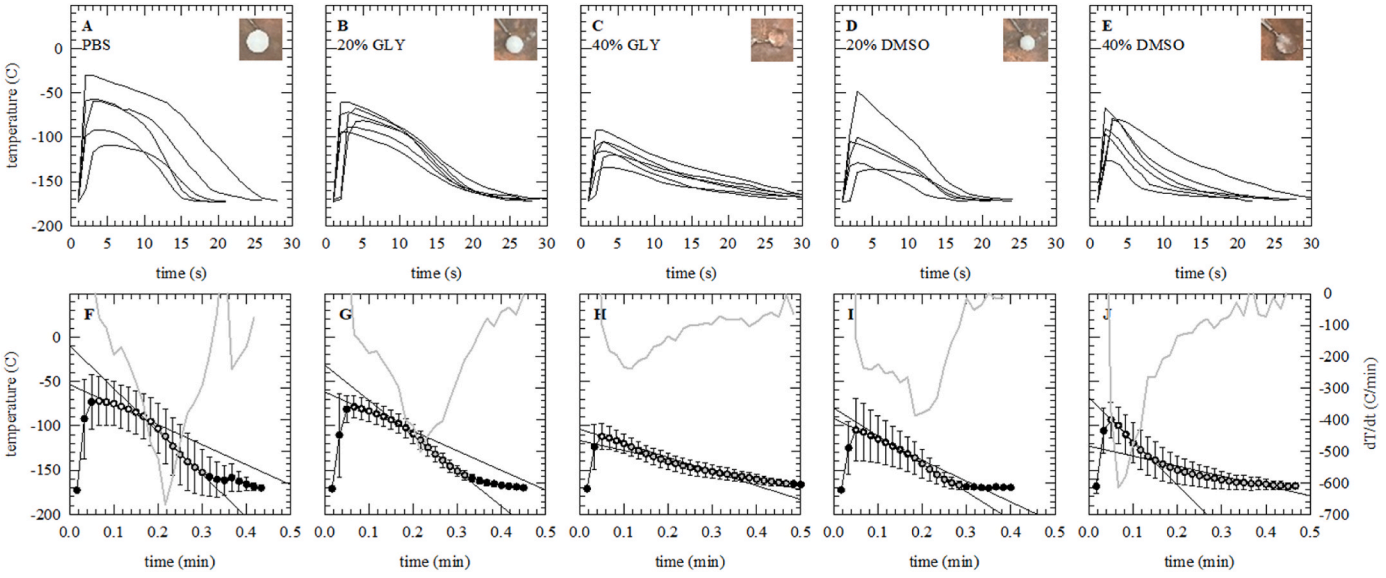

Fig. 4. Experimental assessment of temperature changes occurring in droplets (20-μL) of different compositions during deposition and rapid cooling on a liquid-nitrogen-cooled copper block. A thermocouple was positioned at the cooled block (initial temperature −170 °C), and the temperature was recorded while becoming in contact with the deposited droplet (initial temperature ~22 °C). As solutions were tested: buffered saline (A,F), as well as 20 and 40% GLY (B,C,G,H) or DMSO (D,E,I,J). Representative images depicting frozen/vitrified droplets, as obtained after full cooling for the given solutions, are presented as insets. Panels A–E present single temperature profiles (6 repetitions). Average traces, with standard deviations, are presented in panels F–J. In addition, derivatives (grey lines) and linear regression lines (black lines) were calculated and presented, for illustrating regions with different cooling behavior.

Table 5
Table describing the average time to reach equilibrium temperature (in min), the average cooling rate (in C/min), the minimum derivative of temperature (ΔT) with respect to time (Δt), and the slopes of two linear regressions of PBS, 20%, 40%, GLY and DMSO.

	PBS/-		20% GLY		40% GLY		20% DMSO		40% DMSO	
<-169C; t (min)	0.35	0.07	0.43	0.03	0.54	0.06	0.30	0.04	0.40	0.08
+20>−170C; B (C/min):	562.66	116.10	446.22	32.39	354.89	44.57	641.36	81.25	485.54	88.10
min ([ΔT]/[Δt]); B (C/min):	−710.00	174.17	−401.00	100.72	−269.00	61.82	−458.40	161.42	−530.00	177.45
min ([ΔT]/[Δt]); t (min):	0.23	0.03	0.22	0.03	0.30	0.17	0.20	0.02	0.11	0.04
min ([ΔT]/[Δt]); T (C):	−116.97	20.18	−119.43	9.17	−130.37	17.55	−143.24	15.95	−118.63	21.15
range-1; B (C/min):	−231.39	89.10	−240.91	45.07	−199.13	68.01	−254.25	123.42	−478.10	117.34
range-2; B (C/min):	−562.50	141.72	−431.03	69.21	−102.21	28.42	−368.43	125.64	−166.90	37.52

droplet comes into contact with the thermocouple. The time needed for the sample to reach equilibration (i.e., reaching the temperature of the block) differs for different compositions ranging from 15 to 30 s. The temperature profiles demonstrate distinct phases with varying cooling rates. Samples with a lower CPA concentration that freeze display an initial plateau in the sample temperature, which can possibly be attributed to the density changes at approximately T > −90 °C (Supplementary Fig. 1). Subsequently, fast cooling rates are observed until reaching the equilibrium temperature. In contrast, droplets that undergo vitrification initially exhibit rapid cooling rates followed by a slower cooling phase down to equilibrium. The diminished cooling rate may be due to the increasing density of the vitrified sample as the temperature drops. Derivatives and linear regression lines are added to highlight different phases in the cooling process. Table 5 summarizes the cooling rates in the different phases for samples that freeze and vitrify. Samples that freeze initially show a delayed cooling response, which is not observed in samples that vitrify. In contrast with the simulations, experimental studies suggest that DMSO samples have shorter equilibration times compared to GLY samples.

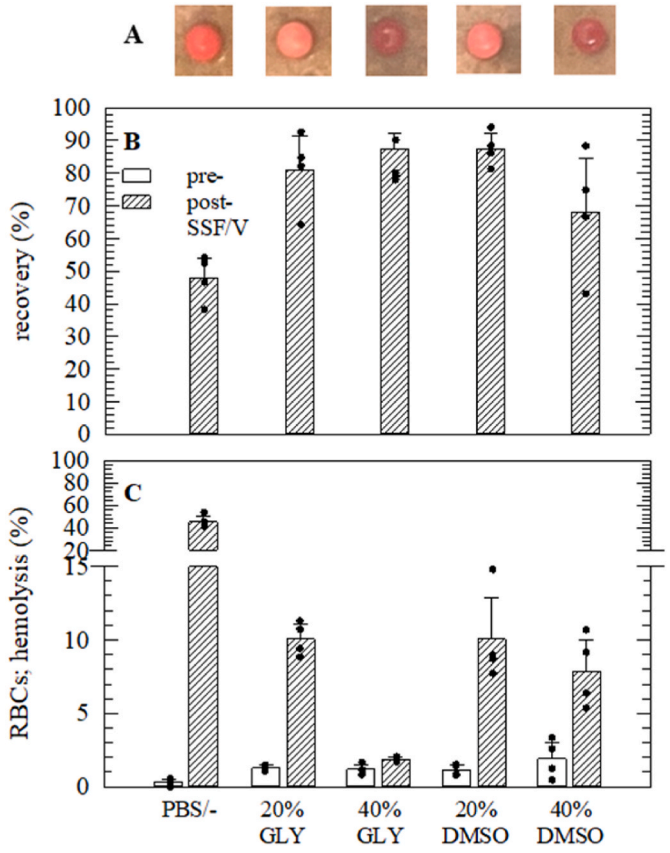

Fig. 5. Experimental outcomes of solid surface freezing/vitrification of 20-μL droplets containing red blood cells (RBCs), i.e., in physiological saline (PBS) without supplements or with presence of 20 or 40% GLY or DMSO. Cell recovery (A) and hemolysis (B) were analyzed as measures for survival, both before subjecting to rapid cooling (white bars) and after thawing/warming (bars with diagonal lines). Averages with standard deviations are presented, determined from four repetitions with different donors, as well as the single data points. (For interpretation of the references to color in this figure legend, the reader is referred to the Web version of this article.)

4.4. Cryopreservation of red blood cells, via rapid cooling in droplets on a cooled surface

SSV/SSF was applied for cryopreservation of RBCs as illustrated in Fig. 5. Physiological buffered saline was used as base medium, while testing GLY and DMSO as CPAs. In the absence of CPAs, only about half of the cells were recovered after freezing-and-thawing (48 ± 6%), and hemolysis increased from 0.3 ± 0.2% before freezing to 46 ± 5% after freezing and thawing. In the presence of 40% GLY, hemolysis was almost entirely prevented and approached the initial pre-freeze values (1.9 ± 0.2%), whereas at 40% DMSO hemolysis was found to be 7.9 ± 2% coinciding with decreased cell recovery values. This indicates that DMSO permeabilizes RBCs at high concentrations, i.e., prior to cooling. In the presence of 20% CPAs similar hemolysis rates were found for GLY and DMSO, of respectively 10 ± 3% and 10 ± 1%. This suggests ultra-rapid freezing results in good cryopreservation outcome. We note that in the absence of CPAs slow freezing (1 °C/min) and even plunging in LN_2 (~300 °C/min) results in virtually 100% hemolysis and <1% recovery. So ultra-rapid freezing results in a relatively good RBC cryopreservation outcome even in the absence of CPAs.

5. Discussion

In this study, heat transfer dynamics during droplet vitrification/freezing on a cold solid surface was simulated using a model. Heat transfer was calculated assuming an isotropic homogeneous medium in a 3-dimensional space using the first law of thermodynamics, where density, heat capacity and thermal conductivity describe the temperature change with time. Solutions of the heat equation are characterized by a gradual smoothing of the initial temperature distribution as heat flows from warmer to colder regions of the droplet driven by temperature gradients. The accuracy of the simulations was verified using experimental measurements of the cooling rate during droplet deposition on a pre-cooled surface.

Both simulations and experimental studies show differences in heat transfer between GLY and DMSO due to inherent differences in material properties of these CPAs. Faster cooling was predicted for GLY droplets due to its greater heat conductivity compared to that of DMSO. In contrast with the heat capacity data of GLY-water, the heat capacity data of DMSO-water were derived from molecular dynamics simulations assuming that DMSO-water systems vitrify. The divergence between the thermal diffusivity values for GLY-water and DMSO-water systems and concomitant differences in heat capacity may explain the predicted differences in cooling rate between GLY and DMSO. We note that the thermal conductivity data in Fig. 2 show a discrepancy for dilute solutions of GLY and DMSO, i.e., at −190 °C for GLY/water at 0% GLY the thermal conductivity is higher than that for DMSO/water at 0% DMSO,

whereas they should be identical. This discrepancy can be attributed to inaccuracies due to extrapolation of the material property data. The experimental studies show shorter equilibration times for DMSO compared to GLY, but differences are minor. Cooling rates of droplets of CPA solutions increase with increasing water contents, which can be attributed to the higher thermal conductivity of ice [40]. The latent heat release during the water to ice phase transition is expected to slow down the cooling, but this effect is not visible in the simulations (Fig. 3) and experimental studies. It should be noted that the latent heat effect can be seen in the simulations, but only when short time steps are used (data not shown). Its effect is almost invisible when the entire cooling process is visualized. In the experimental assessment, the phase transition in samples that freeze occurs during the first second, and hence could not be captured with the setup used here. The different behavior between GLY and DMSO can be attributed to their different structure and groups involved in hydrogen bonds, i.e., restrict the torsional motion of polymer chains, leading to enhanced thermal conductivities [41].

The experimentally determined cooling profiles show several transition points denoting phase or state transitions, which are due to differences in thermal conductivity of liquid, amorphous and crystalline materials. Differences in heat transfer efficiency result from the long-range atomic periodicity in crystalline materials, which allows efficient energy transport by collective motion of molecules (i.e., phonons) [42]. In the amorphous state, the thermal conductivity of DMSO and GLY monotonically decreases with decreasing temperature until the equilibrium temperature is reached. The thermal conductivity of vitrified material appears to smoothly follow the same trend as in the liquid phase. This behavior of vitrified solutions can be attributed to phonon-like collective vibrations of the atoms, which are present but scatter with very short mean free paths. In contrast, the phonon mean free paths in crystals are hundreds to thousands of times their wavelength, leading to larger thermal conductivities [36].

Several limitations need to be noted for both experimental and numerical estimations of cooling rates during droplet deposition on a cold surface. Numerical simulations are dependent on the physical characteristics needed as input. The literature is divergent and incomplete, i.e., with respect to CPA types, concentration, phase state and temperature ranges. Preferably, properties should be derived using similar sample preparation methods and procedures, while using the same equipment. Extrapolation to regions not covered by experimental literature data decreases the accuracy of simulations. Furthermore, physical properties in the vitrified state were not specifically considered, because we found insufficient physical property data of vitrified CPA-water mixtures. In the experimental studies, we were unable to capture the phase transition temperature range due to a lack of sensitivity of the measuring equipment.

The discrepancy in cooling behavior between frozen and vitrified samples can possibly be attributed to differences in density of droplets during crystallization and vitrification, particularly at low subzero temperatures. Density is inversely proportional to thermal diffusivity. In this case, frozen samples have a lower density, resulting in higher thermal diffusivity at $T < 90\ ^{\circ}C$. The shift in thermal diffusivity for GLY mixtures, particularly at temperatures below $-90\ ^{\circ}C$, is shown in Supplemental Fig. 2.

The critical cooling rate (CCR) needed for vitrification depends on the CPA concentration [43]. A plot of the CCR versus the CPA concentration suggests that 20-μL droplets require minimally 40% CPA for vitrification. Oocytes and embryos are typically vitrified at 40% CPA [44,45]. Here we show that RBCs can be preserved by SSV/SSV and to a lesser extent by SSF. Interestingly, even in the absence of CPAs, ultra-rapid freezing already results in a relatively good RBC cryopreservation outcome. Slow freezing or rapid freezing by plunging into LN_2 result in an almost complete loss of cell recovery. Hemolysis can almost entirely be prevented using 40% glycerol. Samples frozen with 40% glycerol appear optically vitrified, but small ice crystal may still be present that can only be detected using X-Ray diffraction measurements. Samples that were ultra-rapidly frozen, i.e., samples with 20% CPA or no CPAs, also show good cryopreservation outcome. In the presence of 20% CPAs, hemolysis rates were found to be approximately 10%. GLY yielded higher cryopreservation outcome comparted to DMSO, which indicates DMSO is less well tolerated than GLY. GLY at 40% is standardly used for RBC cryopreservation, but typically controlled rate slow freezing ($1-5\ ^{\circ}C$/min) is used [46]. Cryopreservation outcome during droplet vitrification/freezing is difficult to compare with that of cryopreserved blood transfusion units because this is done using automated cell processing systems where free hemoglobin is removed. Droplet freezing is not applicable for preservation of blood transfusion units, but may be applicable in disease diagnostics. The dried blood spot method (drying droplets of blood on filter paper) is often used for disease diagnostics, and we envision that spot freezing can be used as alternative. Frozen samples are less prone to oxidative reactions, and solid surface freezing is a relatively simple procedure that does not require specialized equipment.

The numerical simulation model presented here can be used to predict the heat transfer dynamics of droplets exposed to SSV or SSF. Effects of CPA type, CPA concentration and droplet size can be elucidated. The model has been established for GLY and DMSO, but can easily be modified to other CPA types if sufficient material properties are known. Experimental assessment of the cooling rate during SSV/SSF is difficult, and lacks spatial information, i.e., the sample temperature at different positions within the droplet. Nevertheless experimental assessment give additional insights in the cooling dynamics during SSV/SSF.

Acknowledgements

The work described in this study was financially supported via grant WO1735/6–2 and SI1462/4–2 of the German Research Foundation (DFG: Deutsche Forschungsgemeinschaft), and HEMOFORCE (E/U2ED/MD010/LF551, Deutsche Bundeswehr). We kindly acknowledge the Institute for Transfusion Medicine (Hannover Medical School) for providing blood samples.

Appendix A. Supplementary data

Supplementary data to this article can be found online at https://doi.org/10.1016/j.cryobiol.2024.104879.

References

[1] Z. Zhang, Y. Liu, Q. Xing, P. Zhou, Y. Cao, Cryopreservation of human failed-matured oocytes followed by in vitro maturation: vitrification is superior to the slow freezing method, Reprod. Biol. Endocrinol. 9 (2011) 1–6. http://www.rbej.com/content/9/1/156.

[2] M.J. Taylor, B.P. Weegman, S.C. Baicu, S.E. Giwa, Transfus. Med. Hemotherapy 46 (2019) 197–215, https://doi.org/10.1159/000499453. New approaches to cryopreservation of cells, tissues, and organs.

[3] F.S. Trad, M. Toner, J.D. Biggers, Effects of cryoprotectants and ice-seeding temperature on intracellular freezing and survival of human oocytes, Hum. Reprod. 14 (1999) 1569–1577, https://doi.org/10.1093/humrep/14.6.1569.

[4] G.M. Fahy, B. Wowk, Principles of ice-free cryopreservation by vitrification, in: W. F. Wolkers, H. Oldenhof (Eds.), Cryopreservation and Freeze-Drying Protocols. Methods in Molecular Biology 2180, Humana, New York, NY, 2021, pp. 27–97, https://doi.org/10.1007/978-1-0716-0783-1_2.

[5] D.E. Pegg, The role of vitrification techniques of cryopreservation in reproductive medicine, Hum. Fertil. 8 (2005) 231–239, https://doi.org/10.1080/14647270500054803.

[6] Y. Sharma, M. Sharma, Biophysics of cryopreservation, Intl J Thermodynamics 25 (2022) 17–27, https://doi.org/10.5541/ijot.925283.

[7] C.J. Hunt, Cryopreservation: vitrification and controlled rate cooling, in: J. Crook, T. Ludwig (Eds.), Stem Cell Banking, Methods in Molecular Biology 1590, Humana Press, New York, NY, 2017, pp. 41–77, https://doi.org/10.1007/978-1-4939-6921-0_5.

[8] G.M. Fahy, The relevance of cryoprotectant 'toxicity' to cryobiology, Cryobiology 23 (1986) 1–13, https://doi.org/10.1016/0011-2240(86)90013-1.

[9] P.S. Steif, M.C. Palastro, Y. Rabin, The effect of temperature gradients on stress development during cryopreservation via vitrification, Cell Preserv. Technol. 5 (2007) 104–115, https://doi.org/10.1089/cpt.2007.9994.

[10] Y.S. Song, D. Adler, F. Xu, E. Kayaalp, A. Nureddin, R.M. Anchan, R.L. Maas, U. Demirci, Vitrification and levitation of a liquid droplet on liquid nitrogen, Proc. Natl. Acad. Sci. U.S.A. 107 (2010) 4596–4600, https://doi.org/10.1073/pnas.0914059107.
[11] C.C. Pérez-Marín, L. Quevedo, M. Salas, A. Arando, Ultra-rapid freezing using droplets immersed into liquid nitrogen in bull sperm: evaluation of two cryoprotective disaccharides and two warming temperatures, Biopreserv Biobank (2022), https://doi.org/10.1089/bio.2022.0075.
[12] R.J. De Vries, P.D. Banik, S. Nagpal, L. Weng, S. Ozer, T.M. van Gulik, M. Toner, S. N. Tessier, K. Uygun, Bulk droplet vitrification: an approach to improve large-scale hepatocyte cryopreservation outcome, Langmuir 35 (2019) 7354–7363, https://doi.org/10.1021/acs.langmuir.8b02831.
[13] T. Patra, M.K. Gupta, Solid surface vitrification of goat testicular cell suspension enriched for spermatogonial stem cells, Cryobiology 104 (2022) 8–14, https://doi.org/10.1016/j.cryobiol.2021.11.177.
[14] A.A. Malik, K.A. Sofi, A. Khatun, N. Yousuf, Recent advancements in vitrification cryodevices for gamete and gonadal tissue, Cryo Lett. 43 (2022) 129–139, https://doi.org/10.54680/fr22310110112.
[15] D. Pruß, H. Yang, X. Luo, D. Liu, J. Hegermann, W.F. Wolkers, H. Sieme, H. Oldenhof, High-throughput droplet vitrification of stallion sperm using permeating cryoprotective agents, Cryobiology 101 (2021) 67–77, https://doi.org/10.1016/j.cryobiol.
[16] A.R. Moawad, P. Fisher, J. Zhu, I. Choi, Z. Polgar, A. Dinnyes, K.H. Campbell, In vitro fertilization of ovine oocytes vitrified by solid surface vitrification at germinal vesicle stage, Cryobiology 65 (2012) 139–144, https://doi.org/10.1016/j.cryobiol.2012.04.008.
[17] W. Xing, C. Zhou, J. Bian, M. Montag, Y. Xu, Y. Li, T. Li, Solid-surface vitrification is an appropriate and convenient method for cryopreservation of isolated rat follicles, Reprod. Biol. Endocrinol. 8 (2010) 1–9, https://doi.org/10.1186/1477-7827-8-42.
[18] H. Bagis, H. Odaman, H. Sagirkaya, A. Dinnyes, Production of transgenic mice from vitrified pronuclear-stage embryos, Mol. Reprod. Dev. 61 (2002) 173–179, https://doi.org/10.1002/mrd.1144.
[19] A. Maria da Silva, A.G. Pereira, A.V. Brasil, L.B. Macedo, J. Souza-Junior, C. E. Bezerra de Moura, A.F. Pereira, M. Franco de Oliveira, P. Comizzoli, A.R. Silva, Influence of freezing techniques and glycerol-based cryoprotectant combinations on the survival of testicular tissues from adult collared peccaries, Theriogenology 167 (2021) 111–119, https://doi.org/10.1016/j.theriogenology.2021.03.013.
[20] L.E. Ehrlich, Z. Gao, J.C. Bischof, Y. Rabin, Thermal conductivity of cryoprotective agents loaded with nanoparticles, with application to recovery of preserved tissues and organs from cryogenic storage, PLoS One 15 (2020) e0238941, https://doi.org/10.1371/journal.pone.0238941.
[21] B. Wowk, Thermodynamic aspects of vitrification, Cryobiology 60 (2010) 11–22, https://doi.org/10.1016/j.cryobiol.2009.05.007.
[22] J.H. Dymond, Corrected Enskog theory and the transport coefficients of liquids, J. Chem. Phys. 60 (1974) 969–973, https://doi.org/10.1063/1.1681175.
[23] J.S. Feig, P.K. Solanki, D.P. Eisenberg, Y. Rabin, Polarized light scanning cryomacroscopy, part II: thermal modeling and analysis of experimental observations, Cryobiology 73 (2016) 272–281, https://doi.org/10.1016/j.cryobiol.2016.06.004.
[24] T.F. Pijpers, V.B. Mathot, B. Goderis, R.L. Scherrenberg, E.W. van der Vegte, High-speed calorimetry for the study of the kinetics of (de)vitrification, crystallization, and melting of macromolecules, Macromolecules 35 (2002) (2002) 3601–3613, https://doi.org/10.1021/ma011122u.
[25] VDI e.V., VDI-wärmeatlas, Springer Berlin Heidelberg, 2013, https://doi.org/10.1007/978-3-642-19981-3.
[26] L.B. Lane, Freezing points of glycerol and its aqueous solutions, Ind. Eng. Chem. 17 (1925) 924. −924.
[27] R.N. Havemeyer, Freezing point curve of dimethyl sulfoxide - water solutions, J. Pharmaceut. Sci. 55 (1966) 851–853, https://doi.org/10.1002/jps.2600550822.
[28] A. Volk, C.J. Kähler, Density model for aqueous glycerol solutions, Exp. Fluid 59 (2018) 75, https://doi.org/10.1007/s00348-018-2527-y.
[29] L.W. Bosart, A.O. Snoddy, Specific gravity of glycerol, Ind. Eng. Chem. 20 (1928) 1377–1379.
[30] D.A. Jahn, J. Wong, J. Bachler, T. Loerting, N. Giovambattista, Glass polymorphism in glycerol-water mixtures: I. A computer simulation study, Phys. Chem. Chem. Phys. 18 (2016) 11042–11057, https://doi.org/10.1039/C6CP00075D.
[31] Y.C. Yen, Review of Thermal Properties of Snow, Ice, and Sea Ice, US Army, Corps of Engineers, Cold Regions Research and Engineering Laboratory, 1981.
[32] S.A. Schichman, R.L. Amey, Viscosity and local liquid structure in dimethyl sulfoxide-water mixtures, J Phys Chem 75 (1971) 98–102.
[33] S. Fukusako, Thermophysical properties of ice, snow, and sea ice, Int. J. Thermophys. 11 (1990) 353–372, https://doi.org/10.1007/BF01133567.
[34] Glycerine Producers' Association, Physical Properties of Glycerine and its Solutions, 1963.
[35] Engineering ToolBox, 2021. https://www.engineeringtoolbox.com/ice-thermal-properties-d_576.html.
[36] L.E. Ehrlich, J.S. Feig, S.N. Schiffres, J.A. Malen, Y. Rabin, Large thermal conductivity differences between the crystalline and vitrified states of DMSO with applications to cryopreservation, PLoS One 10 (2015) e0125862, https://doi.org/10.1371/journal.pone.0125862.
[37] F.T. Gucker, G.A. Marsh, Refrigerating capacity of two-component systems, Ind. Eng. Chem. 40 (1948) 908–915, https://doi.org/10.1021/ie50461a027.
[38] J. Kim, H. Park, J. Bae, S. Jeong, D. Chang, Investigation of amorphous material with ice for cold thermal storage, Progress in Superconductivity and Cryogenics 20 (2019) 40–44, https://doi.org/10.9714/psac.2019.21.1.040.
[39] J.B. Mandumpal, C.A. Kreck, R.L. Mancera, A molecular mechanism of solvent cryoprotection in aqueous DMSO solutions, Phys. Chem. Chem. Phys. 13 (2011) 3839–3842, https://doi.org/10.1039/c0cp02326d.
[40] W. Doster, A. Bachleitner, R. Dunau, M. Hiebl, E. Lüscher, Thermal properties of water in myoglobin crystals and solutions at subzero temperatures, Biophys. J. 50 (1986) 213–219, https://doi.org/10.1016/S0006-3495(86)83455-5.
[41] L. Zhang, M. Ruesch, X. Zhang, Z. Bai, L. Liu, Tuning thermal conductivity of crystalline polymer nanofibers by interchain hydrogen bonding, RSC Adv. 5 (2015) 87981–87986, https://doi.org/10.1039/C5RA18519J.
[42] D.G. Cahill, R.O. Pohl, Heat flow and lattice vibrations in glasses, Solid State Commun. 70 (1989) 927–930, https://doi.org/10.1016/0038-1098(89)90630-3.
[43] Z. Han, J.C. Bischof, Critical cooling and warming rates as a function of CPA concentration, Cryo Lett. 41 (2020) 185–193.
[44] R. Parnpai, Y. Liang, M. Ketudat-Cairns, T. Somfai, T. Nagai, Theriogenology 86 (2016) 214–220, https://doi.org/10.1016/j.theriogenology.2016.04.034. Vitrification of buffalo oocytes and embryos.
[45] T. Tharasanit, S. Manee-In, S. Buarpung, K. Chatdarong, C. Lohachit, M. Techakumphu, Successful pregnancy following transfer of feline embryos derived from vitrified immature cat oocytes using 'stepwise' cryoprotectant exposure technique, Theriogenology 76 (2011) 1442–1449, https://doi.org/10.1016/j.theriogenology.2011.06.014.
[46] J.W. Lagerberg, Frozen blood reserves, in: W.F. Wolkers, H. Oldenhof (Eds.), Cryopreservation and Freeze-Drying Protocols. Methods in Molecular Biology 2180, Humana, New York, NY, 2021, pp. 523–538, https://doi.org/10.1007/978-1-0716-0783-1_26.